

Antenna In-Situ Performance Analysis for the Hypersonic Flight Vehicle HEXAFLY Employing Measurement Data in a Simulation Model

Björn Möhring, *Student Member, IEEE*, Bernd Gabler, *Member, IEEE* and Markus Limbach

Abstract—An antenna in-situ performance analysis for the hypersonic flight vehicle "HEXAFLY" is presented. Two simulation tools and a Compact Antenna Test Range (CATR) measurement facility are employed to obtain the embedded radiation characteristics of two different antenna systems. In a first step, both antenna types are simulated and measured without the impact of the flight vehicle, but in an environment supporting correct functioning, e.g. on a finite conducting ground plane or on top of a vertical conducting stabilizer. A finite element method (FEM) solver is used for this detailed full-wave analysis of antenna structures with fine geometrical and material details. Next, the FEM solver and a method of moments (MoM) solver with multilevel fast multipole algorithm (MLFMA) acceleration are used to obtain the in-situ radiation characteristic of both antennas mounted on the flight vehicle. The FEM solver is now utilized to simulate the complete setup, whereas the MoM solver works with an equivalent radiation source, which is obtained from CATR measurements of isolated antennas. The results confirm the effectiveness of the measurement data based two-step-approach, which helps to overcome the limitations of pure simulations that are often not feasible for off-the-shelf antennas, and allows the overall validation process to be viewed with added confidence.

Index Terms—Antenna Measurement, Antenna Simulation, Compact Antenna Test Range (CATR), Finite Element Method (FEM), Method of Moments (MoM), Spherical Wave Expansion (SWE).

I. INTRODUCTION

THE HEXAFLY-INT project, as introduced in [1]–[4], is coordinated by ESA-ESTEC and supported by the EU with the objective of designing, manufacturing, assembling, and flight-testing an unpowered high-speed vehicle in a glider configuration. The main focus is on the in-flight testing of several technologies as well as on demonstrating the feasibility of high-speed flight experiments at Mach 7 to 8. The results of the HEXAFLY-INT project will provide the basis for future hypersonic flights to be used in civil long-distance transport. This experimental payload consists of the experimental flight test vehicle (EFTV) with an attached experimental support module (ESM), as seen in Fig. 1. The overall length of this vehicle is close to 4 m and its outer shell is fabricated out of aluminum, copper, titanium, and in parts of ceramic matrix

composite materials. The onboard flight control computer of the EFTV controls the mission management, the guidance, the navigation, the power management, and the telemetry (TM) and telecommand (TC) unit. Since neither the EFTV nor the ESM are planned to be recovered, and the measurement data are not stored in the EFTV, the TM communication link to earth must be established and operate correctly under all flight conditions. The mission control center uses the TC communication system to command the trajectory of the EFTV during its cruise flight. The proper functionality of both communication systems, TM and TC, is crucial for the success of the HEXAFLY-INT project [1]–[4].

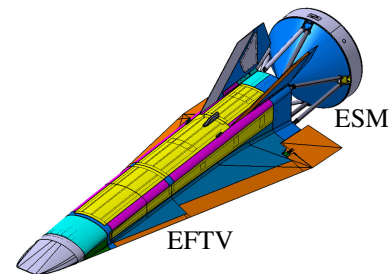


Fig. 1: Flight vehicle consisting of EFTV and ESM.

Antenna placement or antenna in-situ performance analysis on large and complex platforms such as ships, airplanes, satellites, space shuttles or cars has become even more and more important over the years. Different approaches in the area of antenna simulation and measurement have been presented to cope with the different challenges in this field. In [5], the authors propose a hybrid simulation approach consisting of a time-domain full-wave, finite-differences time-domain (FDTD), and a frequency-domain asymptotic method, iterative physical optics (IPO), in order to solve antenna-on-platform problems. The analysis of an antenna mounted on an aircraft is performed in [6]. This analysis is conducted by a domain decomposition method based on the boundary element method (BEM) and the finite element method (FEM). Based on the example of a monopole antenna mounted on an aircraft and on a ship, respectively, the authors of [7] determined the antennas' in-situ performance with a method of moments (MoM) implementation together with the multilevel fast multipole algorithm (MLFMA). For the analysis of electrically large radiation and scattering problems, it is common to use MoM together with the MLFMA as described in [8] and [9]. However, it is not

Manuscript received July 8, 2019; revised May 6, 2020;

The HEXAFLY-INT project was coordinated by ESA-ESTEC and supported by the EU within the 7th Framework Programme Theme 7 Transport Contract no.: ACP0-GA-2014-620327.

B. Möhring, B. Gabler, and M. Limbach are with the German Aerospace Center (DLR), Microwaves and Radar Institute, 82234-Wessling-Oberpfaffenhofen, Germany (e-mail: b.moehring@tum.de)

only pure simulation approaches in the field of antenna-siting problems that have been presented. The authors of [10]–[14] proposed and validated a hybrid technique in which measured antenna data are used as a radiating source in a numerical simulation model. The effectiveness of this method and its applicability for different software tools and different antennas types is described in [12].

This work covers an investigation of the installed antenna performance of the hypersonic EFTV in the project named HEXAFly-INT. It is motivated by the determination of optimal antenna mounting positions for the TM and TC antennas to improve the overall radiation characteristics of the flight vehicle, and to ensure the antenna interoperability.

In the following Section II, the employed methods are introduced and explained, together with the order of investigation in the antenna in-situ performance analysis. This analysis will start with the measurement and simulation of the single TM and TC antennas, and end with the in-situ radiation characteristics of the antennas mounted on the EFTV structure. Section III displays the results of the stand-alone TM and TC antenna performance, whereas Section IV reveals the results of the installed antenna performance on the EFTV structure. In the end in Section V, results of the proposed method are recalled and compared.

II. FORMULATION OF METHODS AND ANALYSIS CONCEPT

This section introduces the methods deployed in this antenna in-situ performance analysis, as well as the concept and order of the analysis. The simulation tool ANSYS HFSS (ANSYS Electronics Desktop 2017.2) [15] uses a 3-D, full-wave, frequency-domain electromagnetic field solver based on the FEM [16] for the simulation of the antennas or any given electromagnetic problem. The antenna design framework (ADF) by IDS [17] of version 5.1, the second simulation tool employed, makes use of a MoM code [18] together with the MLFMA [19], which uses the combined field integral equation (CFIE) formulation of Maxwell's equations [20], [21]. The ADF reads antenna far-field pattern data from measurements, converts the data by SWE, and uses this data as a radiating source in the numerical simulation model.

In this study, the measurement data are acquired in the CATR, which is operated by the German Aerospace Center (DLR) in Oberpfaffenhofen, Germany. Insights, working principle, and measurement quality of this facility can be found in [22] and [23]. The frequency-domain processing technique known as Mathematical Absorber Reflection Suppression (MARS) as introduced in [24] is employed to correct the measurement data and to improve the accuracy of this CATR. The measurement and post-processing tool Antenna and Radar Cross Section (ARCS) Measurement System [25] from the manufacturer of the CATR, March Microwave System B.V., is used for the acquisition of the measurement data and for transformation of the measured far-field patterns into a near-field source employing a SWE.

Solutions of Maxwell's equations in spherical coordinates can be represented by Hankel functions of the second kind (radial dependence r), Legendre functions (polar dependence

ϑ), and an exponential function (azimuthal dependence φ) when assuming a time-harmonic field according to $e^{j\omega t}$. In the case of the TE solution, the resulting vector function $\mathbf{M}_{m,n}^4(\mathbf{r})$ represents the electric field and includes two vector components that are tangential to the spherical surface. The TM vector function $\mathbf{N}_{m,n}^4(\mathbf{r})$ for the electric field also contains a radial vector component. The total radiated field in general form $\mathbf{E}(\mathbf{r})$ can be expressed as a linear combination of these vector wave functions with their weighting coefficients $S_{m,n}^1$ and $S_{m,n}^2$:

$$\mathbf{E}(\mathbf{r}) = \frac{k}{\sqrt{\eta}} \sum_{n=1}^{\infty} \sum_{m=-n}^n [S_{m,n}^1 \mathbf{M}_{m,n}^4(\mathbf{r}) + S_{m,n}^2 \mathbf{N}_{m,n}^4(\mathbf{r})] \quad (1)$$

The electric field $\mathbf{E}(\mathbf{r})$ can be calculated in any location as the sum of spherical vector waves that are centered to the source, if these coefficients were available. This method is known as SWE and is often applied in spherical near-field antenna measurements. In practice, there is a cut-off criterion for the infinite summation in (1). Considering the radial wave impedance as a ratio of electric and magnetic field components, these impedances are mainly resistive in a region that contributes to the radiated field, when $n < kr$. The variable k represents the wavenumber, $k = 2\pi/\lambda$, whereby λ is the wavelength, and the variable r the radius. The free-space impedance is denoted by η in (1). Whereas in the case of $n > kr$, the impedances are reactive and these higher-order modes are evanescent. For the determination of the cut-off, a safety margin takes some higher-order modes into account to include all significantly radiated energy in the solution. In far-field ranges or CATRs, which by nature only measure radiated fields, higher-order modes originate from multiple reflections and can be excluded, if solely the physical dimensions of the antenna under test (AUT) with all its radiating components are known. As a consequence, this technique allows a de-embedding of an antenna from support structures and from equipment outside the minimum radial sphere that encloses the radiator [26]–[28]. The ADF-tool analyzes the structural influence of the EFTV on the overall radiation characteristics of the TM and TC antennas. In the two-step-approach, it processes actual measurement data from the antenna as measured in the CATR, converts it into a near-field source for the simulation model employing the SWE and uses this data in a MoM simulation model for obtaining the antenna in-situ performance. This approach is more realistic than a pure simulation since it works with measured data. Moreover, it offers a cheaper and simpler alternative in contrast to in-situ measurements of the antennas mounted on a full-scale electromagnetically equivalent mock-up of the EFTV. The pure simulation of the installed antenna performance often suffers from the limited availability of exact antenna design parameters. In some cases, the antenna design data remains undisclosed deliberately due to IP reasons. With the suggested two-step-approach, elaborate reverse-engineering to obtain the antenna design parameters becomes superfluous and can be replaced by simple measurements.

In the following, the order and strategy are described as to how this antenna in-situ investigation of the HEXAFly

vehicle is approached. First, the individual performance of the TC and the TM antenna is simulated using HFSS. In order to consider the actual environment of the antennas on the EFTV, the TM antenna is mounted in one setup over a finite conducting ground plane and in a second setup on top of a conducting vertical stabilizer. Due to aerodynamic constraints, the mounting position of the TC antenna is restricted to the EFTV fuselage. Therefore, the TC antenna is simulated over a finite conducting ground plane only. The same configurations are also used for the measurement of the antenna models in the CATR to ensure comparability. A rudder mock-up and a ground plane made of aluminum are built for testing antennas in the two working environments. The left half of the schematic in Fig. 2 illustrates this analysis and comparison approach. Simulation results of the TC and TM antenna being mounted over a finite ground plane are compared to the CATR measurement results of the same configuration. The right half of the chart in Fig. 2 describes the in-situ performance evaluation by comparing MoM and FEM results when the TC and TM antenna is mounted on the structure of the EFTV model. Herein, the MoM simulation employs measurement results from the CATR of the TC and TM antenna over a ground plane employing a SWE, as indicated by a blue arrow in Fig. 2. The results of the TC and TM antenna over a ground plane are presented in Section III-A and III-B respectively, while the results of the in-situ performance of the TC and TM antennas are shown in Section IV-A and IV-B. In the second setup, the radiation characteristics of the TM antenna are investigated first on the tip of a stand-alone vertical stabilizer and subsequently on the tip of the vertical rudder of the EFTV. Fig. 3 presents a chart of the analysis approach for this case. The radiation characteristics of the TM antenna mounted on the top of a vertical stabilizer is simulated in HFSS using the FEM, and compared to the results obtained by the CATR, in which the TM antenna is measured on top of a vertical stabilizer mock-up. The results are shown in Section III-C, while Section IV-C covers the comparison of the MoM results with FEM results when the TM antenna is placed on a vertical stabilizer of the EFTV model.

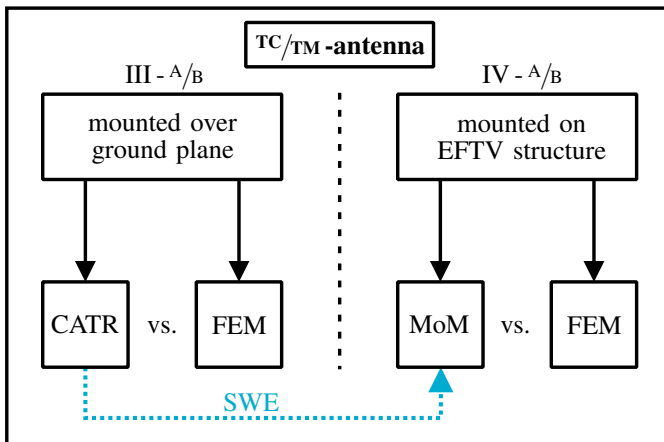


Fig. 2: Analysis and comparison approach of TC and TM antenna mounted on ground plane and on EFTV structure, respectively.

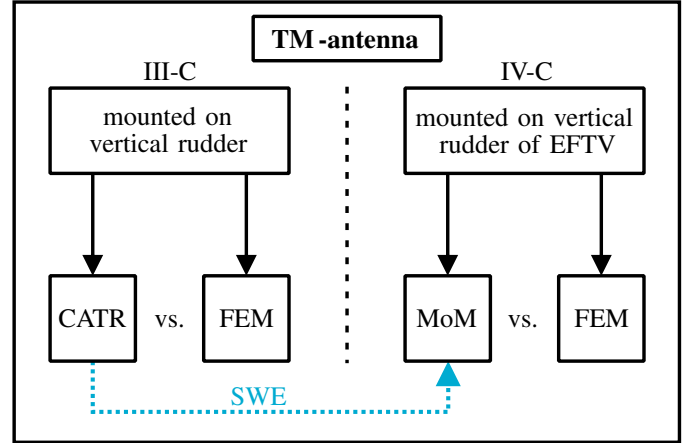


Fig. 3: Analysis and comparison approach of TM antenna mounted on vertical rudder mock-up and on vertical rudder of EFTV structure.

III. ANTENNA CHARACTERISTICS ANALYSIS

This section deals with the analysis and investigation of the TC and TM antenna installed on a finite ground plane and, in the case of the TM antenna, also installed on top of a vertical stabilizer. The results of the two methods, FEM and CATR, are compared as indicated on the left-hand side of the charts in Figs. 2 and 3. Both antennas radiate linearly polarized fields. In order to quantify and evaluate the performance of the antennas, we analyze the far-field gain distribution of each setup in terms of co- (CO) and cross-polarized (CX) field components [29]. In terms of the Ludwig Type 3 coordinate system, we refer to the CO and CX components of the field as Ludwig-III-X (L-III-X) and Ludwig-III-Y (L-III-Y) in accordance with our measurement and simulation setups.

A. Telecommand (TC) Antenna

The TC antenna used here is an airborne instrumentation antenna manufactured by TECOM Industries of type 1050002B, S/N 3017, as depicted in Fig. 4. This antenna is certified, approved, and successfully tested for such space- and airborne applications with respective temperature requirements. The center frequency of this antenna is stated to be at 449.95 MHz. A mechanical CAD model describing the shape



Fig. 4: TC antenna type 1050002B, S/N 3017, by TECOM Industries.

of this Inverted-F type TC antenna in STEP format and a test sheet with an input-matching plot are provided by TECOM Industries. Material parameters, internal Ohmic, and dielectric losses of the electrically short antennas are not available. A 3D-simulation model assuming no internal losses in the antenna was designed from CAD data and tuned to meet the desired center frequency with tolerable antenna port matching.

Information about the interior is based on back-engineering by DLR-RB-MORABA [30] and remains undisclosed. The TC antenna, mounted on a finite ground plane and placed on the positioner of the CATR, is shown in Fig. 5. Here, the TC antenna is interfaced with a 30 cm square aluminum plate to a 1.4 m square ground plane. This smaller plate is flush-mounted with the larger plate and ensures better interchangeability of the antenna from the large host ground plane. The edges of the ground plate are equipped with pyramidal foam absorbers to minimize diffraction effects. The pattern is measured at a

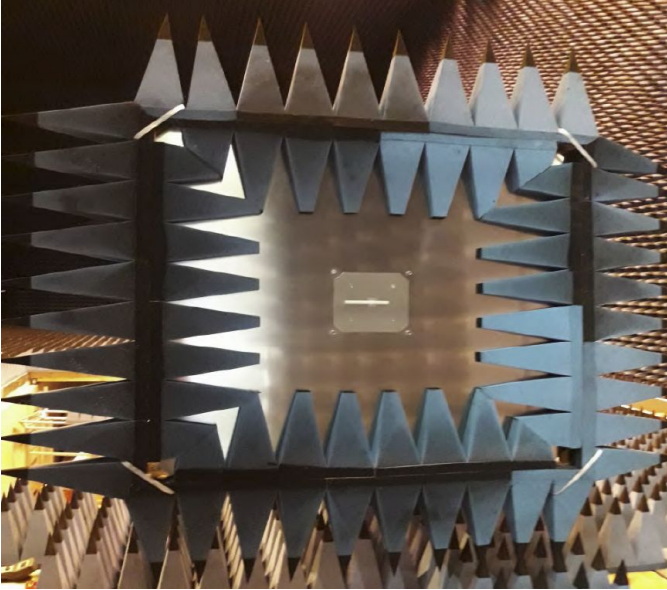


Fig. 5: TC antenna mounted on square ground plane in CATR.

frequency of 450 MHz in the CATR. In this case, the radiation characteristics cover a full sphere due to back-radiation effects and the finite size of the ground plane. At this frequency, the diameter of the ground plate corresponds to an electrical length of about 2λ . In comparison to the infinite ground plane used in the HFSS simulation model, the electrical size of the ground plate in the CATR setup is significantly smaller, which impacts the radiation behavior of this configuration. A comparison of simulated and measured results is depicted in Fig. 6. Here, the gain distribution of the CO components in the two principal cuts ($\varphi = 0^\circ$, $\varphi = 90^\circ$) are plotted against the elevation angle ϑ . However, these gain results do not consider the unknown Ohmic and dielectric losses of the antenna because they were also excluded from the FEM simulation model. On the other hand, the polarization and mismatch losses are taken into account. Directivity is calculated from pattern integration of the measured spherical data. Due to reasons of comparability, measurement results also include polarization and mismatch losses, as seen in Fig. 6. Because of the boundary condition in the simulation model of an infinite ground plane, the elevation angle ϑ cannot exceed $\pm 90^\circ$, whereas the measurement results cover a total sphere ($\vartheta = \pm 180^\circ$). Considering the effect of the non-ideal and electrically small ground plane in the measurement setup, there is still an agreement between the measurement and the simulation results, especially in the region of ($\vartheta = \pm 60^\circ$). Due

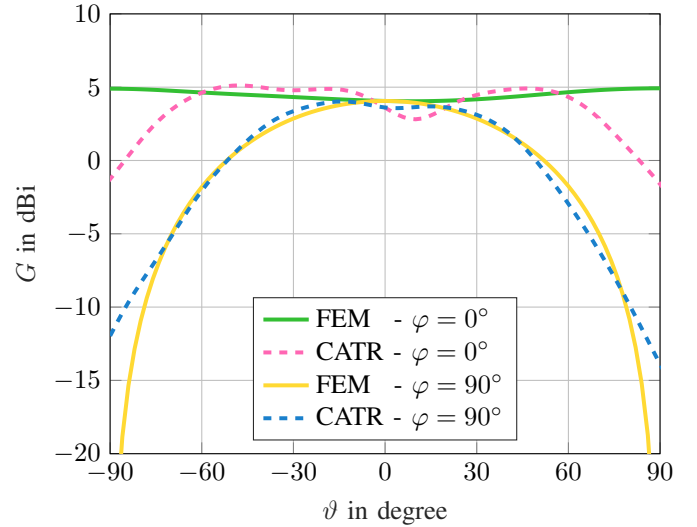


Fig. 6: Simulated and measured gain distribution of TC antenna mounted on ground plane in principal cuts.

to the different boundary conditions, the agreement between the two results is lost when the elevation angle ϑ approaches $\pm 90^\circ$. In addition to this, the absorbing material with its finite thickness attached to the ground plane as seen in Fig. 5 also contributes to a reduction in gain for the CATR results for ϑ -values approaching $\pm 90^\circ$.

B. Telemetry (TM) Antenna

The antenna used for the TM communication on the EFTV is also of the Inverted-F type. This TM antenna with a center frequency of 2.3 GHz is designed by DLR-RB-MORABA [30] and is usually operated in commonly launched ballistic research rockets. Like the TC antenna, this antenna is also certified and approved for such space-borne and airborne applications. A photo of the antenna is shown in Fig. 7. A CAD model and all material parameters are provided by DLR-RB-MORABA [30]. The simulation with HFSS is performed at a



Fig. 7: TM antenna with coaxial feed by DLR-RB-MORABA [30].

frequency of 2.3 GHz, and considers all material parameters and dimensions as supplied by the manufacturer. This time, the internal losses of the antenna of about 1.2 dB are also considered in both, simulation and measurement. The setup in the CATR is shown in Fig. 8 and resembles the setup of the TC antenna. Due to the frequency of operation of 2.3 GHz, the diameter of the plate now has an electrical length of about

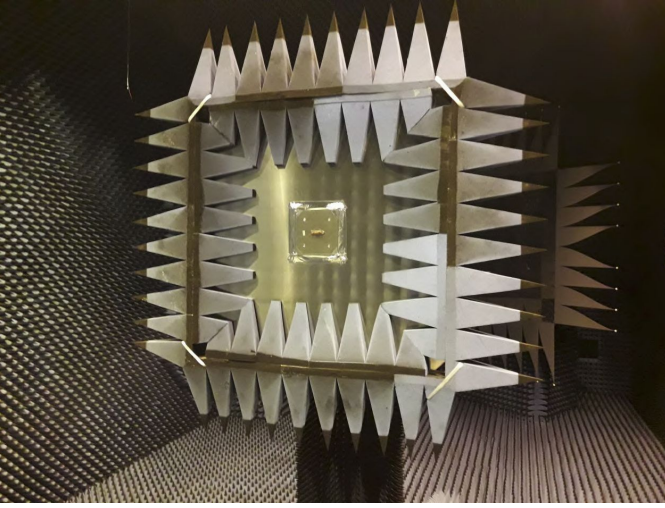


Fig. 8: TM antenna mounted on square ground plane in CATR.

11λ . The electrical size of the ground plane in the case of the TM antenna is about five times larger than in the case of the TC antenna of Fig. 5. Both the simulation results of HFSS together with the measurement results of the CATR of the TM antenna over a conducting ground plane are plotted in Fig. 9. The realized gain by the CO components in the principal cuts ($\varphi = 0^\circ$, $\varphi = 90^\circ$) is displayed as a function of the elevation angle ϑ . Analysis of the two methods indicates the effect of the theoretically perfectly conducting infinite ground plane in the simulation, compared to the imperfectly conducting and limited-in-size aluminum ground plate in the measurement. The plots in Fig. 9 show good agreement between the FEM simulation with the CATR measurements, especially for the $\varphi = 90^\circ$. As in the previous case with the TC antenna, the simulation model of the TM antenna also considers only half of the sphere ($\vartheta = \pm 90^\circ$) due to the boundary conditions of an infinite ground plane. The difference in the two setups is

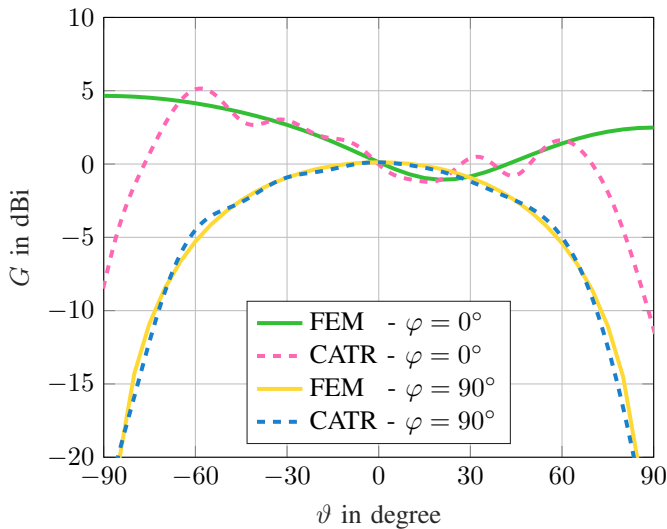


Fig. 9: Simulated and measured gain distribution of TM antenna mounted on ground plane in principal cuts.

the reason for the difference between the two plots of the cut in $\varphi = 0^\circ$ in Fig. 9 when exceeding the angle of $\vartheta = \pm 60^\circ$. As in the case of the TC antenna, the absorbing material with its finite thickness attached to the ground plane as seen in Fig. 8 reduces the gain values for ϑ exceeding $\pm 60^\circ$.

C. Telemetry (TM) Antenna on Vertical Stabilizer

The two rear vertical stabilizers (vertical rudders) are potential mounting positions for the TM antenna on the EFTV. In order to investigate the in-situ performance of the TM antenna placed on top of a vertical stabilizer, simulations with HFSS and measurements with the CATR are carried out and their results compared, as indicated on the left-hand side of the schematic in Fig. 3. A model or mock-up of the vertical stabilizer is built of aluminum according to the dimensions of the actual rudder of the EFTV. The Fig. 10 shows the mechanical CAD model of this mock-up that was imported to HFSS for the simulation. The simulation is performed at a frequency of 2.3 GHz. A photo of the measurement setup with the TM antenna mounted on the mock-up of the vertical stabilizer in the CATR is shown in Fig. 11. Pyramidal foam absorbers are employed to minimize the edge- and back-scattering effects of the mock-up. A comparison of the simulation and measurement results of this TM antenna configuration is depicted in Fig. 12 and Fig. 13. It can be seen that the values from the measurement are close to those of the FEM simulation. It should be noted that the exact position of the various ripples is influenced by multiple parameters, and might easily be the cause of a gain variation of ± 1 dB. These ripples arise predominantly due to higher-order modes that occur as a result of the antenna rudder mock-up configuration. The whole mock-up structure with its rims, edges, and slits contributes to the overall radiation characteristic. The correspondence is lost when the angle ϑ exceeds $\pm 130^\circ$. This is caused by the different boundary conditions of the simulation and measurement setup, respectively. The FEM simulation model assumes free-space conditions, whereas the measurement setup in the CATR provides free-space conditions only in the upper hemisphere. When inspecting the results of the lower hemisphere, at angles of $\vartheta = \pm 110^\circ$ to $\vartheta = \pm 180^\circ$, two attributes of the CATR come into effect. Signal blockage and attenuation

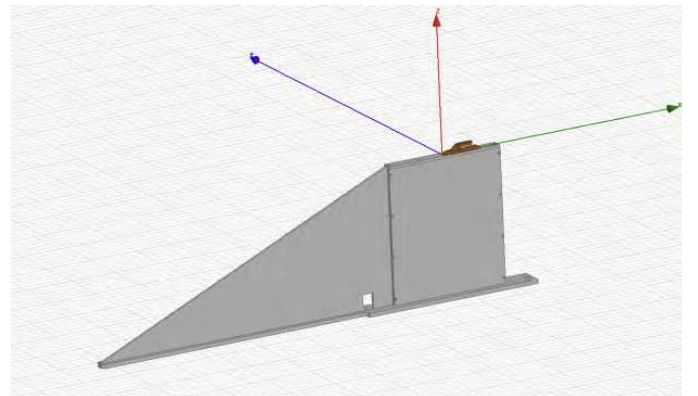


Fig. 10: Simulation model of TM antenna mounted on top of vertical stabilizer mock-up.



Fig. 11: TM antenna mounted on top of vertical stabilizer mock-up in CATR.

occurs due to the presence of the positioner of the CATR with its absorbing material, together with the attenuating effect of the absorbing material around and on the rear side of the rudder mock-up as seen in Fig. 11, and on and around the finite ground plane model as shown in Fig. 5 and Fig. 8. These two reasons cause a significantly lower gain in the lower hemisphere regarding the CATR results. Furthermore, these results illustrate how sensitive the wide beam of the TM antenna is to its environmental structure. A high consistency is noticeable when summarizing the previous results of both the simulation and measurement of the two antenna types in the given environment for values of $\vartheta = \pm 135^\circ$, i.e. the upper hemisphere. This validates the measurement setup and the simulation model. Explanations for deviations can be found in the different boundary conditions, the lack of information regarding the TC antennas' material, and mechanical parameters, discretization, and numerical errors of the simulation tool HFSS, as well as in the amplitude and phase variations in the quiet zone (QZ) of the CATR. The QZ exhibits amplitude variations of up to ± 0.5 dB, phase variations of up to $\pm 5^\circ$ and a CX isolation of typically -40 dB and more. The deviations in

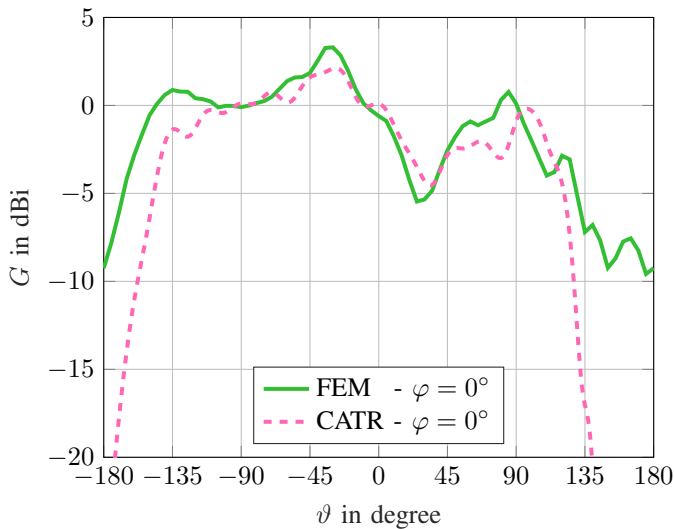


Fig. 12: Simulated and measured gain distribution of TM antenna mounted on vertical stabilizer mock-up at $\varphi = 0^\circ$.

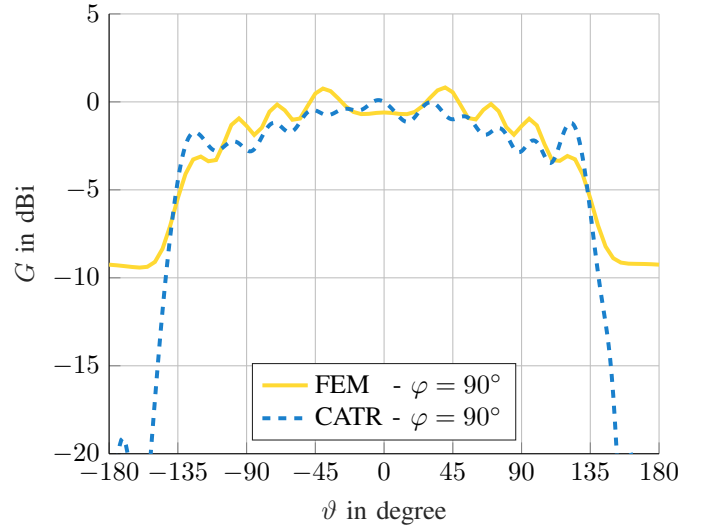


Fig. 13: Simulated and measured gain distribution of TM antenna mounted on vertical stabilizer mock-up at $\varphi = 90^\circ$.

the two mounting structures (ground plane, vertical stabilizer mock-up) of the simulation CAD model compared to the fabricated parts for the CATR measurements, are also a factor attributing to the different results. This rudder mock-up is not ideal, and is fabricated out of several different aluminum plates, not offering a uniform and yet finite conductivity and revealing small slits along the structure as well. Furthermore, connectivity issues arise from the flush mounting of an antenna made out of copper to a small ground plate made of aluminum.

IV. IN-SITU ANTENNA PERFORMANCE ON EFTV

Now, the influence of the EFTV structure on the overall radiation characteristic is analyzed. Three different antenna positions on the EFTV structure are investigated. This in-situ radiation performance is simulated with FEM in HFSS and with MoM in ADF. In ADF, a triangular mesh was employed and the mesh size was set to $\lambda/6$ to $\lambda/8$. In HFSS the simulations were performed with a tetrahedral mesh, radiating boundary conditions on all faces, and an airbox enclosing the EFTV. In delicate and sensitive areas the mesh was refined and adapted locally.

A. Telecommand (TC) Antenna

For the TC antennas, the two rear mounting positions are investigated, as indicated in Fig. 14. These positions are chosen preferably due to aerodynamic reasons. The rear position ensures a better air flux along the fuselage and prevents unwanted air vortices. In the reference coordinate system as shown in Fig. 14, the direction of flight is set to be in the direction of the x-axis. The local coordinate systems of the CATR and the FEM simulation model match. For the installed performance evaluation of the antennas, these coordinate systems are transformed to match the global coordinate system of the EFTV as seen in Fig. 14. The electrical size of the EFTV, in terms of wavelength, exhibits a length of about 6λ at the simulation frequency of 450 MHz. The impact of

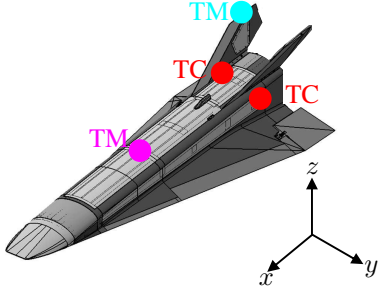


Fig. 14: EFTV model with indicated mounting positions for the two TC antennas, one TM antenna on the center fuselage (pink dot), and one TM antenna on vertical stabilizer (cyan dot).

the EFTV structure on the overall radiation characteristics is plotted in Fig. 15 for the two principal cuts. Here, the simulation results from the FEM code are compared against the MoM results. The structural impact of the EFTV on the radiation characteristics is apparent and the two curve pairs exhibit great similarity. In order to find the optimal mounting

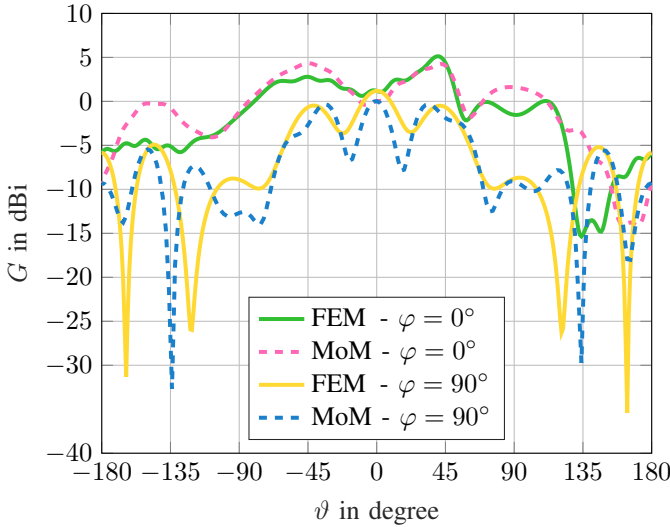


Fig. 15: Simulated gain distribution of two TC antennas mounted on EFTV model in principal cuts.

position of the TC antennas, for the calculation of the radio link budget and to identify possible unexpected dips in the radiation pattern, the overall 3D radiation pattern is of interest. Therefore, the gain distribution of the MoM results in a 3D radiation pattern representation is seen in Fig. 16. Since the internal losses of the TC antenna are unknown and therefore not considered in the simulation model, as described in Section III-A, they are also ignored in the measured results from the CATR for the MoM simulation. Measurements show that the internal Ohmic and dielectric losses are on the order of approximately 3.3 dB. However, in the link budget calculation, these losses were indeed taken into account.

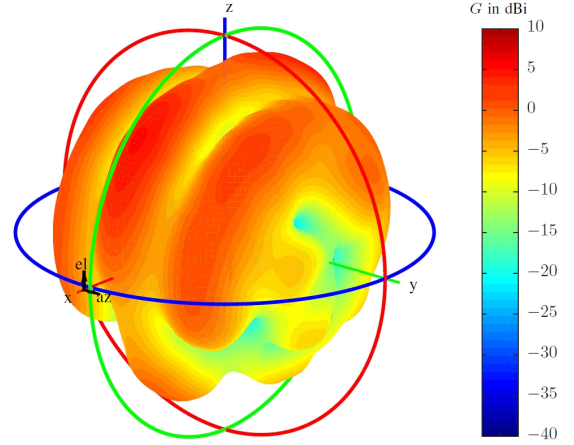


Fig. 16: Simulated gain distribution of two TC antennas mounted on EFTV in 3D radiation pattern representation.

B. Telemetry (TM) Antenna in Center Position

The in-situ performance of a single TM antenna on the EFTV structure is investigated in this section. First, in Subsection B, the center position on the fuselage is tested, as depicted in Fig. 14 by the pink dot, while in Subsection C the results of one TM antenna mounted on the vertical stabilizer are presented, as indicated by the cyan dot in Fig. 14. The frequency in the simulation is again set to 2.3 GHz. The surface currents as induced by the equivalent source of the TM antenna placed on the center position of the fuselage are depicted in Fig. 17 and reveal the electrical length of over 30λ . The current distribution is obtained via the MoM code and indicates significant currents on the antenna's mounting position in the center, but also along the wing edges, at the rear vertical stabilizer, and at the tip of the fuselage. Besides, the wave propagation along the structure emanating from the center is easily visible. The way that the structure of the EFTV

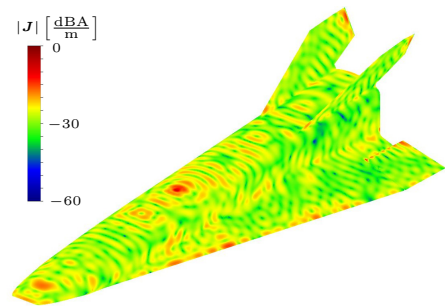


Fig. 17: Normalized surface currents $|\mathbf{J}|$ on EFTV caused by TM antenna mounted in the center of the EFTV.

affects the radiation characteristics of the TM antenna is seen in Fig. 18 and Fig. 19. These two plots show the simulation results of the FEM and the MoM codes. The Savitzky-Golay filter [31] is applied in order to smooth the results by reducing the ripples to achieve easier readability in the two figures. The Savitzky-Golay filter uses a local least-squares polynomial approximation to achieve a smoothing of the noisy experimental data, while preserving the width and height of peaks in the signal waveform [32]. These results can be compared with

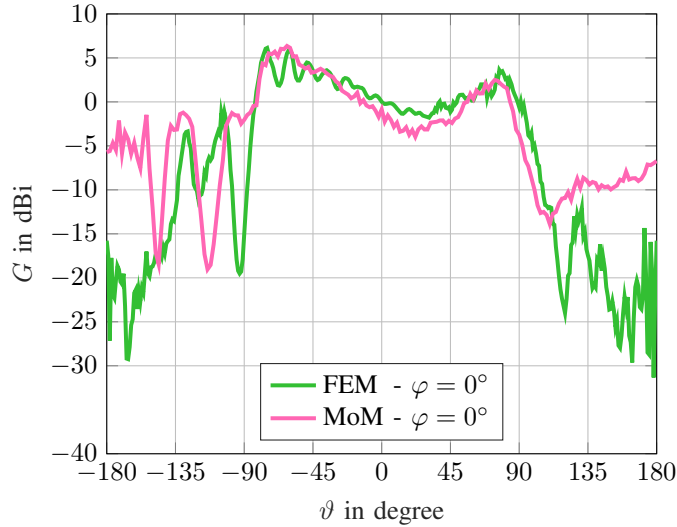


Fig. 18: Simulated gain distribution of the TM antenna mounted on top of the EFTV model at $\varphi = 0^\circ$.

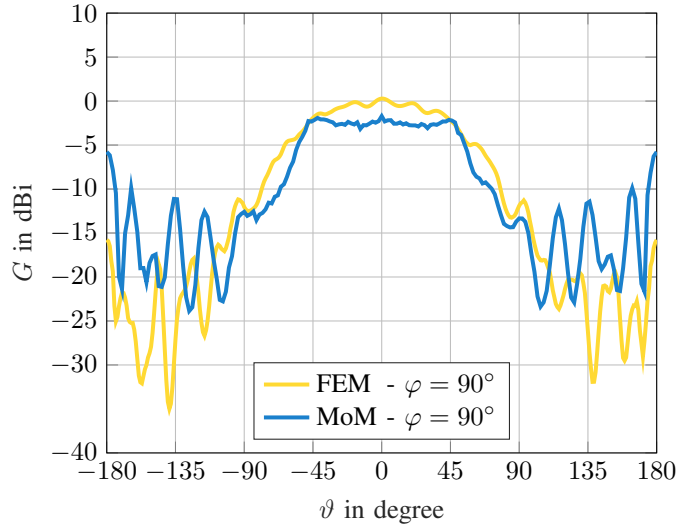


Fig. 19: Simulated gain distribution of the TM antenna mounted on top of the EFTV model at $\varphi = 90^\circ$.

the plots in Fig. 9 that display the gain distribution of the TM antenna over a conducting ground plane. FEM and MoM results of Fig. 18 and Fig. 19 show a high consistency. The correlation decreases when exceeding $\vartheta = \pm 100$ degrees. In this case, the MoM indicates a higher gain than the FEM results primarily due to the different boundary conditions as explained in Section III. To offer a more comprehensive view of the overall radiation performance, Fig. 20 shows a 3D radiation pattern representation of the gain distribution of the MoM results.

C. Telemetry (TM) Antenna on Vertical Stabilizer

The top of the EFTV rear vertical stabilizer is another possible mounting position for the TM antenna, as indicated by the cyan dot in Fig. 14. This position is favored due to aerodynamic and electromagnetic requirements. The Fig. 21

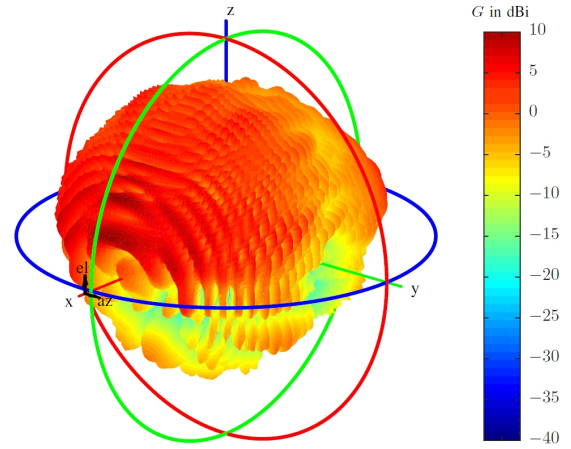


Fig. 20: Simulated gain distribution of TM antenna mounted on EFTV in center position in 3D radiation pattern representation.

illustrates the surface current distribution on the structure of the EFTV model, as induced by the TM antenna mounted on the tip of the rear vertical stabilizer. Especially along the rims and the edges of the stabilizer, the current exhibits far greater values compared to the rest of the structure. The gain distribution in the main cuts obtained with FEM and MoM are depicted in Fig. 22 and Fig. 23, respectively. Here, the results from the simulation are again smoothed using the Savitzky-Golay filter, to ensure a better readability. A 3D radiation pattern presentation of the MoM results is shown in Fig. 24.

The trend in the two components of Fig. 22 reveals a level

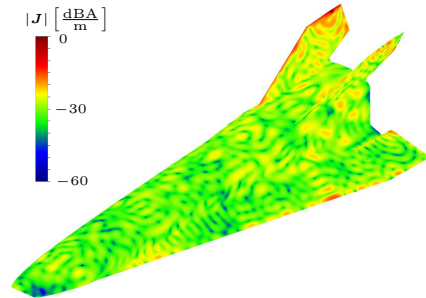


Fig. 21: Normalized surface currents $|J|$ on EFTV caused by TM antenna on right vertical stabilizer.

of similarity. Except for the center region of $\vartheta = \pm 20^\circ$, MoM results indicate a higher gain throughout, in contrast to the FEM outcome for the previous cases. When comparing the two results for the $\varphi = 90^\circ$ in Fig. 23, a consistency is noticeable, except for the center region of $\vartheta = \pm 20^\circ$ and for the region from $\vartheta = 60^\circ$ to $\vartheta = 180^\circ$. The structural impact of the mounting structure on the radiation pattern is visible when comparing the 3D patterns of the Fig. 20 and Fig. 24. The two sets of results of the TM antenna mounted on the rear vertical stabilizer, as seen in the final step, are not fully comparable. There, the comparison overall of the pure simulation (FEM) with the two-step-approach (CATR and MoM) was very good. It must be taken into account that the differences in the gain distributions regarding the lower hemisphere of the stand-alone antennas, as described towards the end of Section III, are conveyed to the results of the antennas installed on the

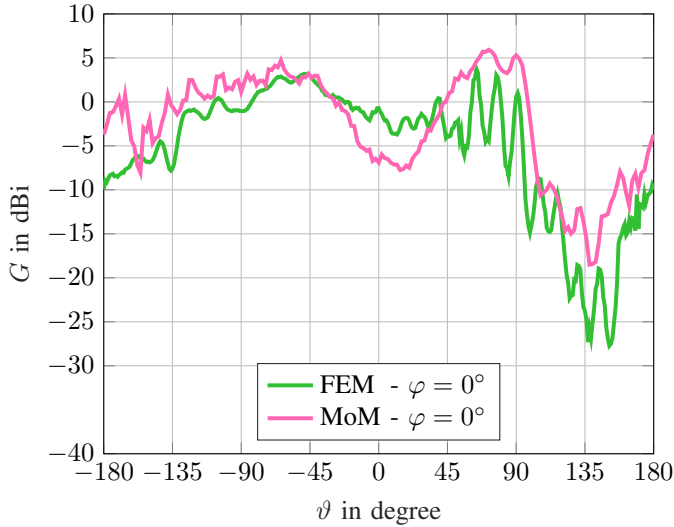


Fig. 22: Simulated gain distribution of TM antenna mounted on vertical stabilizer of EFTV model at $\varphi = 0^\circ$.

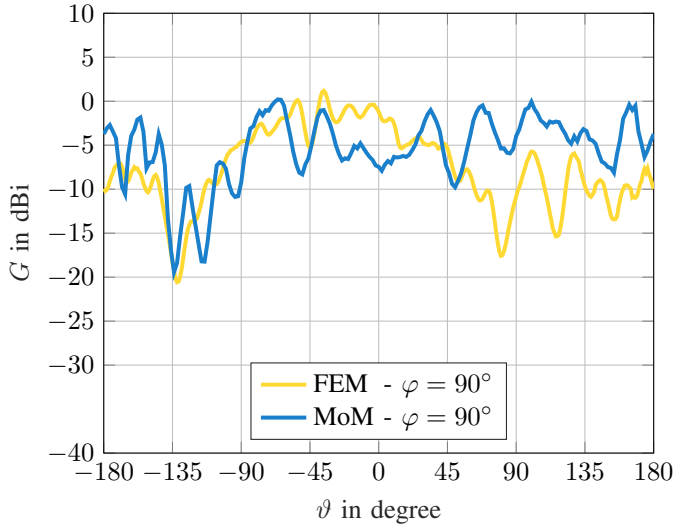


Fig. 23: Simulated gain distribution of TM antenna mounted on vertical stabilizer of EFTV model at $\varphi = 90^\circ$.

EFTV. Another explanation for these deviations is found in the two different measurement environments. The measurements of the Sections IV-A and IV-B were conducted over a finite conducting ground plane, whereas the measurement of Section IV-C was conducted on a narrow vertical stabilizer. The radii of the minimum sphere applied in the SWE differ greatly between the two measurement cases. In the case of the plate, the minimum sphere radius is significantly smaller because the spherical modes offering the most energy and thus contributing most to the radiation, are centered and concentrated at the mounting position of the antenna. In the case of the antenna being mounted on the vertical stabilizer, the minimum sphere radius is nearly twice as large, because the whole and oblong rudder structure with its many edges and rims contributes to the radiation and therefore needs to be taken into account. Hence, the number of modes to consider is significantly larger,

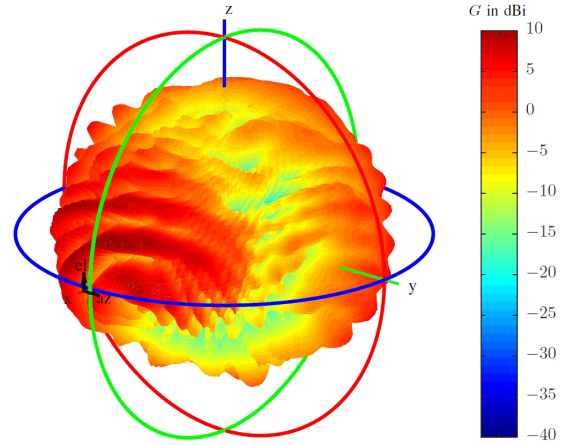


Fig. 24: Simulated gain distribution of TM antenna mounted on EFTV rudder in 3D radiation pattern representation.

and they are not as concentrated within this sphere as in the case of the plate. Mode truncation is performed according to [26] in order to exclude modes that do not originate from the antenna investigated and which would falsify the measurement results. However, this mode truncation is as well a potential source of error in the SWE when modes are excluded which would impact the radiation behavior in a correct manner. Furthermore, an additional error could have arisen from a different interpretation of the mechanical as well as electromagnetic mesh in the two simulation tools, and may have caused disagreements in the results of Section-IV-C. It was a difficult task to transfer, import, and mesh the EFTV model between the two simulation tools. In this process, differences may have occurred in the geometrical structure, and hence in the corresponding mesh in the two different simulation models. The successful meshing of a structure like a vertical stabilizer with its rims, edges, and slits is a more difficult task than meshing an even and smooth rectangular plate. Regarding the mission constraints, the configuration of the two TC antennas at the rear mounting position and the center position of one single TM antenna on top of the EFTV vehicle has been chosen. These decisions were made in cooperation with ESA-ESTEC based on the proposed method of working with measured antenna sources in a simulation model (MoM+SWE). This method allows for a prompt evaluation of various mounting positions and saves valuable time and expenses that would be spent on a complete EFTV mock-up design, the manufacturing, and in-situ antenna testing. About 85,000 € could be saved on the design of a complete EFTV mock-up employing this method.

V. CONCLUSION

In the example case of the hypersonic flight vehicle HEX-AFLY, the antenna in-situ performance of different antennas and different mounting positions has been investigated. The antenna's radiating behavior was determined with two simulation tools, HFSS (FEM) and ADF (MoM+MLFMA) and with a CATR for measurements. For the proof of concept, the results of these methods were compared and discussed. The similarity of the FEM simulation results with the respective

measurement results in the CATR was very high for both setups, with the two antennas being mounted on a conducting plane and on top of a vertical stabilizer. The results of the presented two-step-approach of utilizing measured antenna patterns employing a SWE as a radiating source in a MoM simulation model were compared against a full FEM simulation model. The results of the FEM simulation provided support and verification only, whilst the decisions regarding the antenna mounting positions across the whole project are based on the results of the proposed two-step-approach. It was seen that the agreement between the two methods was high concerning the mounting position on the rear side of the fuselage regarding the TC antenna, and on top of the center fuselage on the EFTV with regard to the TM antenna. This presented two-step-approach offers a novel approach of solving antenna-siting problems, and ensures a higher accordance with reality, since it works with measured data.

ACKNOWLEDGMENT

The authors would like to thank Johan Steelant from ESA-ESTEC, Alexander Kallenbach from DLR MORABA, Pol van de Coevering from March Microwave Systems B.V., and Giancarlo Guida from IDS Ingegneria Dei Sistemi S.p.A. for providing support, assistance, and technical insights.

REFERENCES

- [1] S. Di Benedetto, M. Di Donato, A. Rispoli, S. Cardone, J. Riehmer, J. Steelant, and L. Vecchione, "HEXAFly-INT Project: Design of a High Speed Flight Experiment," *World Academy of Science, Engineering and Technology, International Journal of Mechanical, Aerospace, Industrial, Mechatronic and Manufacturing Engineering*, vol. 10, no. 5, pp. 915–921, 2016.
- [2] J. Steelant, T. Langener, K. Hannemann, M. Marini, L. Serre, M. Bouchez, and F. Falempin, "Conceptual Design of the High-Speed Propelled Experimental Flight Test Vehicle HEXAFly," in *20th AIAA International Space Planes and Hypersonic Systems and Technologies Conference*, 2015, p. 3539.
- [3] G. Pezzella, M. Marini, B. Reimann, and J. Steelant, "Aerodynamic Design Analysis of the HEXAFly-INT Hypersonic Glider," in *20th AIAA International Space Planes and Hypersonic Systems and Technologies Conference*, 2015, p. 3644.
- [4] J. Steelant, V. Villace, A. Kallenbach, A. Wagner, J.-Y. Andro, S. Di Benedetto, B. Saracoglu, S. Chernyshev, A. Gubanov, V. Talyzin, N. Voevodenko, N. Kukshinov, A. Prokhorov, N. Grigoriev, A. Neely, D. Verstraete, and D. Buttsworth, "Flight Testing Designs in HEXAFly-INT for High-Speed Transportation," in *International Conference on High-Speed Vehicle Science and Technology (HISST)*, Moscow, Russia, Nov. 2018.
- [5] B. Le Lepvrier, R. Loison, R. Gillard, P. Pouliguen, P. Potier, and L. Patier, "A New Hybrid Method for the Analysis of Surrounded Antennas Mounted on Large Platforms," *IEEE Transactions on Antennas and Propagation*, vol. 62, no. 5, pp. 2388–2397, 2014.
- [6] A. Barka and P. Caudrillier, "Domain Decomposition Method Based on Generalized Scattering Matrix for Installed Performance of Antennas on Aircraft," *IEEE Transactions on Antennas and Propagation*, vol. 55, no. 6, pp. 1833–1842, 2007.
- [7] X.-W. Zhao, X.-J. Dang, Y. Zhang, and C.-H. Liang, "The Multilevel Fast Multipole Algorithm for EMC Analysis of Multiple Antennas on Electrically Large Platforms," *Progress In Electromagnetics Research*, vol. 69, pp. 161–176, 2007.
- [8] X. Wang, Z. Peng, K. Lim, and J. Lee, "Multisolver Domain Decomposition Method for Modeling EMC Effects of Multiple Antennas on a Large Air Platform," *IEEE Transactions on Electromagnetic Compatibility*, vol. 54, no. 2, pp. 375–388, April 2012.
- [9] U. Jakobus, J. van Tonder, and M. Schoeman, "Advanced EMC Modeling by Means of a Parallel MLFMM and Coupling with Network Theory," in *IEEE International Symposium on Electromagnetic Compatibility EMC*, 2008, pp. 1–5.
- [10] L. Foged, L. Scialacqua, F. Saccardi, J. A. Quijano, G. Vecchi, and M. Sabbadini, "Practical Application of the Equivalent Source Method as an Antenna Diagnostics Tool [AMTA Corner]," *IEEE Antennas and Propagation Magazine*, vol. 54, no. 5, pp. 243–249, 2012.
- [11] L. Foged, L. Scialacqua, F. Saccardi, F. Mioc, D. Tallini, E. Leroux, U. Becker, J. A. Quijano, and G. Vecchi, "Bringing Numerical Simulation and Antenna Measurements Together," in *8th European Conference on Antennas and Propagation (EuCAP)*. IEEE, 2014, pp. 3421–3425.
- [12] L. Foged, L. Scialacqua, F. Saccardi, and F. Mioc, "Measurements as Enhancement of Numerical Simulation for Challenging Antennas," in *9th European Conference on Antennas and Propagation (EuCAP)*. IEEE, 2015.
- [13] L. Foged, M. Saporetti, M. Sierra-Castanner, E. Jørgensen, T. Voigt, F. Calvano, and D. Tallini, "Measurement and Simulation of Reflector Antenna," in *9th European Conference on Antennas and Propagation (EuCAP)*. IEEE, 2015, pp. 1–5.
- [14] M. Saporetti, L. Scialacqua, F. Saccardi, L. Foged, J. Zackrisson, D. Trenta, and L. S. Drioli, "Validation of Measured Source Antenna Representation in the Numerical Simulation of a GNSS Antenna on Sentinel Satellite," in *Antenna Measurement Techniques Association Symposium (AMTA)*, 2017, pp. 1–4.
- [15] ANSYS, Inc., "HFSS - High Frequency Structural Simulator," 2016. Canonsburg, PA, USA. [Online]. Available: <http://www.ansys.com/Products/Electronics/ANSYS-HFSS>, accessed on May 5, 2020.
- [16] J.-M. Jin, *The Finite Element Method in Electromagnetics*. John Wiley & Sons, 2015.
- [17] IDS Ingegneria Dei Sistemi S.p.A., "ADF - Antenna Design Framework," 2016. Pisa, Italy. [Online]. Available: <https://www.idscorporation.com/pf/space-electromagnetic-solutions/>, accessed on May 5, 2020.
- [18] W. C. Gibson, *The Method of Moments in Electromagnetics*. CRC Press, 2014.
- [19] J. Song, C.-C. Lu, and W. C. Chew, "Multilevel Fast Multipole Algorithm for Electromagnetic Scattering by Large Complex Objects," *IEEE Transactions on Antennas and Propagation*, vol. 45, no. 10, pp. 1488–1493, 1997.
- [20] M. Sabbadini, G. Guida, and M. Bandinelli, "The Antenna Design Framework - ElectroMagnetic Satellite," *IEEE Antennas and Propagation Magazine*, vol. 51, no. 2, pp. 225–235, April 2009.
- [21] G. Galgani, G. Guida, M. Sabbadini, M. Bandinelli, and P. Di Bartolomeo, "Antenna Design Framework: Solving the EDA Antinomy," in *5th European Conference on Antennas and Propagation (EuCAP)*. IEEE, 2011, pp. 2839–2843.
- [22] M. Limbach, B. Gabler, R. Horn, and A. Reigber, "DLR-HR Compact Test Range Facility," in *3rd European Conference on Antennas and Propagation (EuCAP)*. IEEE, 2009, pp. 2186–2189.
- [23] B. Möhring, M. Limbach, B. Gabler, and A. Di Maria, "Modular Simulation of a Compact Antenna Test Range," in *11th European Conference on Antennas and Propagation (EuCAP)*. IEEE, 2017, pp. 2576–2580.
- [24] S. Gregson, J. Dupuy, C. Parini, A. Newell, and G. Hindman, "Application of Mathematical Absorber Reflection Suppression to Far-Field Antenna Measurements," in *Loughborough Antennas and Propagation Conference (LAPC)*. IEEE, 2011, pp. 1–4.
- [25] MARCH Microwave System B.V., "Antenna and Radar Cross Section Measurement System (ARCS)," 2017. Nuenen, Netherlands.
- [26] S. Gregson, J. McCormick, D. J. Van Rensburg, and C. Parini, *Theory and Practice of Modern Antenna Range Measurements*. The Institution of Engineering and Technology, 2014.
- [27] A. Ludwig, "Near-Field Far-Field Transformations Using Spherical-Wave Expansions," *IEEE Transactions on Antennas and Propagation*, vol. 19, no. 2, pp. 214–220, 1971.
- [28] Y. Lopez, C. Cappellin, F. Las-Heras, and O. Breinbjerg, "On the Comparison of the Spherical Wave Expansion-to-Plane Wave Expansion and the Sources Reconstruction Method for Antenna Diagnostics," *Progress In Electromagnetics Research*, vol. 87, pp. 245–262, 2008.
- [29] A. Ludwig, "The Definition of Cross Polarization," *IEEE Transactions on Antennas and Propagation*, vol. 21, no. 1, pp. 116–119, 1973.
- [30] German Aerospace Center (DLR), "Mobile Rocketbase (MORABA)," accessed on May 5, 2020. [Online]. Available: <https://www.moraba.de/>
- [31] A. Savitzky and M. J. Golay, "Smoothing and Differentiation of Data by Simplified Least Squares Procedures," *Analytical Chemistry*, vol. 36, no. 8, pp. 1627–1639, 1964.
- [32] R. W. Schafer, "What is a Savitzky-Golay Filter," *IEEE Signal Processing Magazine*, vol. 28, no. 4, pp. 111–117, 2011.